Probing the biological identity of Inorganic Nanoparticles with anomalous Small Angle X-ray Scattering

Marvin Skiba,[1,2,†] Lars Klemeyer,[1,2,†] Gabriela Guedes,[3] Xiao Sun,[4] Sylvio Haas,[4] Aitziber L. Cortajarena,[3,5] Dorota Koziej,[1,2] Wolfgang J. Parak,[1,2] Carlos Sanchez-Cano *[5,6,7]

[1] Center for Hybrid Nanostructures, University of Hamburg, 22761 Hamburg, Germany.
[2] The Hamburg Centre for Ultrafast Imaging, 22761 Hamburg, Germany.
[3] Center for Cooperative Research in Biomaterials (CIC biomaGUNE), Basque Research and Technology Alliance (BRTA), 20014 Donostia-San Sebastian, Spain.
[4] Deutsches Elektronen-Synchrotron DESY, Notkestr. 85, Hamburg 22607, Germany
[5] Ikerbasque, Basque Foundation for Science, 48013 Bilbao, Spain
[6] Donostia International Physics Center, 20018 Donostia-San Sebastian, Spain
[7] Polimero eta Material Aurreratuak: Fisika, Kimika eta Teknologia, Kimika Fakultatea, Euskal Herriko Unibertsitatea UPV/EHU, 20018 Donostia-San Sebastian, Spain,
E-mail: carlos.sanchez@dipc.org
† These authors contributed equally to this work.

Abstract:

In a biological milieu, nanoparticles (NPs) undergo alterations that go from aggregation or degradation to the adsorption of a corona of proteins. Those changes influence significantly the intrinsic properties and biological capacities of the engineered nanomaterials, and need to be fully understood for successful biomedical use of NPs. We used synchrotron anomalous small-angle X-ray scattering (ASAXS) to probe the individual SAXS contributions from the different components of NPs (core, polymeric coating, and protein corona) on several in vitro systems. By applying a model-based fitting approach combined with pair distance distribution analysis, we were able to investigate whether and to what extent proteins formed a corona around different nanoparticles. The results obtained agree with well-established dynamic light scattering and transmission electron microscopy experiments, confirming the capacity of ASAXS to obtain full information from complex NP samples, and opening for its use in more realistic biological environments.

Introduction:

Nanoparticles (NPs) are interesting tools towards the development of biomedical agents. Some NP-based formulations have already been approved by regulatory agencies for use in drug delivery or as contrast agents, allowing their introduction into clinical practice and the broader context of daily life.[1–4] However, several challenges still need to be addressed regarding *in vivo* application, including those linked to biologically induced alterations to the structure or stability of NPs.[5] In the case of inorganic NPs, the NPs are typically composed of an inorganic core (metal, metal oxide, semiconductor, etc.) surrounded by a layer of organic ligands, usually consisting of organic polymers. Size and shape of the NPs are fundamental parameters directly influencing the biological response following the administration *in vivo* or *in vitro* of the particles. Among others, the size and shape of NPs are closely related to *in vivo* clearance (*e.g.* increased renal filtration for small NPs) and cellular uptake (*e.g.* by modulating interaction with cell membranes).[6–10] The ligand layer enhances the colloidal stability and solubility of NPs, but also passivates their surface to reduce the reactivity. Those ligands direct the interaction between the NPs and biomolecules, and can be engineered to enhance their biocompatibility. As such, the nature of the polymers used can affect cell internalisation and tissue penetration, achieve targeted delivery or reduce the immune response of the organism after administration of the nanomaterial.[11–13] Additionally, following the introduction of the NPs into a biological fluid, their surface is coated by a variety of proteins, lipids, and/or other biological macromolecules.[14] This dynamic protein corona also influences drastically biodistribution, cellular uptake, and biocompatibility.[15–19] In this way an inorganic NP in biological environment can be conceptually segmented into its inorganic core, is ligand shell, and the corona of adsorbed biological molecules.[20]

In view of this, it is clear that changes in any of those three components during *in vivo* use can alter the nature of the interaction between a NP-based biomedical agent and the organism, affecting its clinical efficiency. Therefore, it is essential to probe any change in core, ligand layer and protein corona individually to fully understand the real pharmacological properties of NPs after administration.[20] Ideally, a single method capable of being applied both at the cellular level and in whole animal models would be desired.

While a number of *ex vivo* techniques, including dynamic light scattering (DLS) or transmission electron microscopy (TEM) can be used to characterise NP cores, ligand layers and protein coronas, there is a need for the development of techniques that can probe those components *in vivo*.[21–23] Notably, chromatographic techniques cannot be utilised directly *in vivo* due to their nature, and optical methods in the UV-visible range (*e.g.* DLS or fluorescence microscopy) are

limited to surface areas of the organism because of tissue absorption. TEM only can be applied to extracted samples. Nuclear magnetic resonance (NMR), and radioactive labelling techniques like positron emission tomography (PET) and single-photon emission computed tomography (SPECT) are capable of tracking the fate of the core, ligands and the protein corona around NPs, both *in vitro* and *in vivo*. [24–26] However, PET and SPECT do not provide structural information on each of the components, and NMR does it but only through long acquisitions that make the technique unsuitable for *in vivo* applications.

Alternatively, X-ray-based techniques like X-ray fluorescence imaging (XFI) or wide/small angle X-ray scattering (WAXS/SAXS) have also been used to study the different components of NPs in biology.[27,28] Such techniques can be used for imaging at the cellular level and scaled up for use in larger model systems.[29,30] Moreover, they can be applied to optically opaque samples like tissues or full organisms, and permit to achieve different penetration depending on the energy of the X-rays used.[31–33] Therefore, X-ray techniques are good candidates as single methods to probe NPs both *in vitro* and *in vivo*. For instance, XFI can provide element-specific maps with excellent spatial resolution.[34,35] We have recently shown that introducing exogenous labels enables us to track the intracellular fate of the protein corona around AuNPs.[27] However, it does not provide any structural information on the alterations of the NPs size and shape induced by biological aggregation or degradation. Equally, scattering techniques, such as SAXS can provide valuable information about the overall shape, size, and homogeneity of NPs.[36,37] However, SAXS is unable to differentiate details from individual components, as the technique averages the scattering contributions from the different layers of the sample and obscures their specific characteristics.[31,32]

The objective of our study is to demonstrate the potential of anomalous small-angle X-ray scattering (ASAXS) as a valid technique for differentiating between the individual components of NPs. ASAXS exploits the variations in scattering that occur near the absorption edges of specific elements, where the scattering factors change significantly due to resonant interactions between the incident X-ray photons and the electrons in the sample.[38–40] This provides element-specific contributions, which can enable the extraction of scattering information from each layered segment of the NP system if they are significantly different in their elemental composition. As such, ASAXS has been employed to assess the individual sizes of the different components of the core of multimetallic NPs.[41,42] Initial ASAXS studies also yielded promising results to differentiate between the inorganic core and polymer ligands of NPs.[43] However, we demonstrate here an extension of this approach to the third layer, the protein

corona, that was made possible by the introduction of tags with high-Z elements onto the different layers to enhance the accuracy of the method.

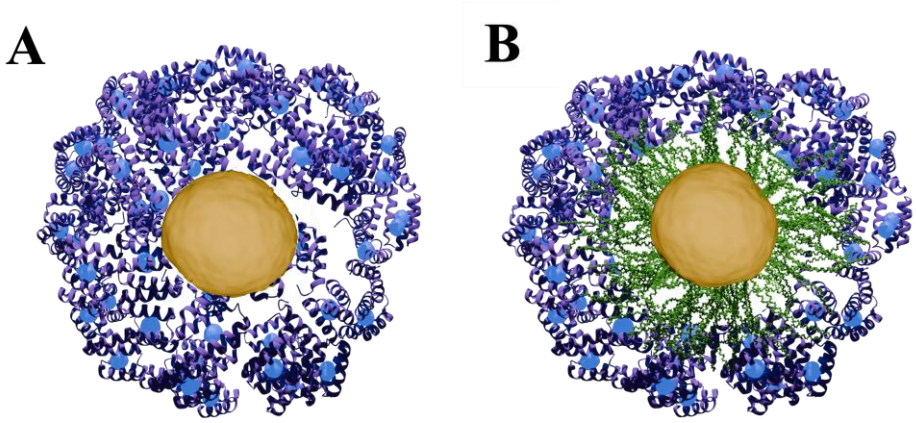

Scheme1: Illustration showing the different formulations of AuNP studied in this publication. A) AuNPs (gold) carrying Gd-labelled proteins (purple) covalently immobilised onto their surface to form a continuous shell, were used as a positive control. B) In parallel, we coated AuNPs with combinations of biomedically relevant organic surfactant (polyethylene glycols - PEGs, shown in green) before introducing the Gd-labelled proteins. Bromine labelling of the PEG allowed us to assess simultaneously the size of AuNP, PEG, and the surrounding proteins.

Results and Discussion

2.1. Nanoparticle synthesis and conventional characterisation

A small library of Au NPs sharing the same 12 nm Au core was generated. Particles were coated with 3 kDa polyethylene glycol (PEG) carrying amino terminal groups (**AuNP@PEG-NH_2**), 2 kDa PEG carrying bromine terminal groups (**AuNP@PEG-Br**) or a combination of both (75% amino- and 25% bromine-terminated PEG respectively; **AuNP@PEG-mix**) to obtain NPs with diverse surface properties. Finally, a NP carrying a stable protein corona was generated by binding a recombinant designed consensus tetratricopeptide repeat (CTPR) protein,[44–47] labelled with Gd, to the Au core through an engineered unique C-terminal cysteine (**AuNP@CTPR-cys-Gd**). This was created as a positive control for the formation of the protein corona.

Particles were generated using two different batches of Au cores prepared following the same protocol,[48] and presented minor discrepancies in their size and zeta potential. Therefore, results presented herein discriminate between the two batches. Transmission electron microscopy (TEM) analysis confirmed that both sets of NP cores exhibited a narrow size distribution, with diameters d_c of 12.0 ± 0.9 nm (number of investigated NPs: N = 634) for batch 1 and 12.6 ± 0.7 nm (N = 107) for batch 2 (Figure 1 A, B, D, E). Although the number of NPs evaluated for batch 2 was lower, a resampling analysis of NPs in batch 1 (implementing a random value picker to select 107 from the 643 NPs available, and performing 20 iterations) confirmed that this sample size is sufficient to represent the size distribution (*cf.* SI chapter 1, Figure S1 and Table S1). The successful functionalisation of AuNPs with the different ligand layers was indicated by a slight shift in the localised surface plasmon resonance (LSPR) peak following the replacement of the citrate capping agents with PEG or protein molecules (Figure 1 C, F). Furthermore, laser Doppler anemometry was employed to track alterations in ζ-potential after surface modification. For batch 1, the initial citrate-capped AuNPs exhibited a zeta-potential ζ of -18.5 ± 0.6 mV, was unchanged (-18.9 ± 2.8 mV) after covalent functionalisation with **CTPR-cys-Gd**, and changed to +26.3 ± 1.0 mV or -0.9 ± 0.9 mV after modification with PEG-NH_2 or PEG-Br (respectively). In the second batch, the ζ-potential exhibited a shift from an initial value of -11.6 ± 2.4 mV (citrate-capped) to a final value of +8.6 ± 0.6 mV following modification with the 75% amino- and 25% bromine-terminated PEG mixture. This suggests the formation of a mixed ligand layer, as the zeta potential is placed between that of fully amine- and fully bromine-terminated PEG coatings.

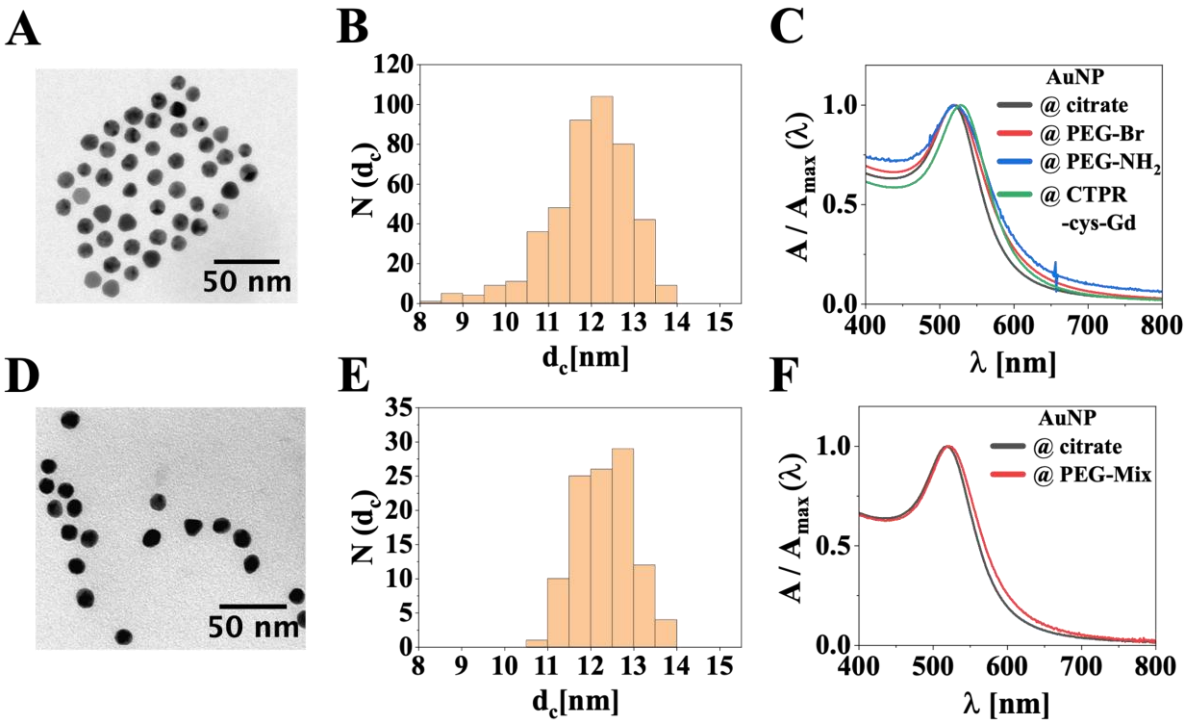

Figure 1: Colloidal characterisation of the two NP batches used in this study. A, B, C) batch 1; D, E, F) batch 2. A, D) Representative transmission electron microscopy (TEM) images of the AuNPs, showing their narrow size distribution and spherical morphology. Scale bar: 50 nm. B, E) Histograms showing the distribution frequency $N(d_c)$ of AuNPs core diameters (d_c) as determined from TEM images, N = 634 for B), N = 107 for E). C, F) Normalised UV-visible absorption spectra $A/A_{max}(\lambda)$ of the AuNPs highlighting spectral shifts due to different surface modifications.

2.2. Protein corona formation and characterisation

To investigate normal non-covalent adsorption of proteins around AuNPs, we also expressed a variant of the **CTPR-cys-Gd** protein that lacked the terminal cysteine but maintained the same Gd label (**CTPR-Gd**). This protein, with computed dimensions of approximately 9.9 nm (length, L_{prot}) by 3.8 nm (width, d_{prot}) (Figure S2),[40] was used to form the corona around the pegylated AuNPs studied in our experiments. The new **CTPR-Gd** protein could no longer bind covalently to AuNPs via the terminal cysteine, but maintained an overall negatively charge. Thus, it could be adsorbed electrostatically to the positively charged amino-terminated PEG, mimicking a native-like protein corona that could be detected by X-rays techniques thanks to the Gd labelling.[27] Then, the hydrodynamic diameter d_h of all NPs was evaluated in the absence or presence of **CTPR-Gd** proteins using DLS. As is the case of TEM (similar d_c), also the volume-weighted DLS measurements showed similar hydrodynamic diameters d_h of

12.9 ± 0.2 nm and 13.1 ± 0.7 nm for the Au cores of batch 1 and batch 2 (respectively; *cf*. Figure 2).

Direct covalent immobilisation of **CTPR-cys-Gd** proteins onto AuNPs *via* thiol-gold coupling increased the hydrodynamic diameter of the particle to $d_{h,\ core+prot}$ = 29.0 ± 1.0 nm (Figure 2A). Considering that the computed length of one stretched protein *is ca.* 9.9 nm, the increase in size observed is in agreement with the formation of a monolayer of proteins axialy oriented around the AuNPs. Further inductively-coupled-plasma mass-spectrometry (ICP-MS) analysis of **AuNP@cys-CRPT-Gd** determined that 70.7 ± 2.0 CTPR proteins were bound per AuNP (considering the size and lattice of the AuNPs and the labelling efficiency of Gd per protein). Moreover, this allowed to extrapolate a theoretical 6.4 nm^2 footprint of **CTPR-cys-Gd** proteins on the AuNPs surface, which is slightly smaller than one would expect for the 3.8 nm width of the protein. Possibly because the protein is anchored solely through its terminal cysteine and adopts a more stretched orientation on the curved nanoparticle surface, thus reducing the effective footprint.[#]

Equally, DLS showed that the hydrodynamic diameter of **AuNPs@PEG-NH_2**, **AuNPs@PEG-mix** and **AuNPs@PEG-Br** increased respectively to $d_{h,\ core+PEG}$ = 26.8 ± 0.3 nm, 28.5 ± 1.0 nm and 21.7 ± 0.6 nm (Figure 2B-D) after coupling of the PEGs to the AuNPs. The reduced size of **AuNPs@PEG-Br** compared to the other NPs was expected, as PEG-Br (2 kDa) is smaller than PEG-NH_2 (3 kDa). Incubation of the PEGylated AuNPs with **CTPR-Gd** proteins resulted in increases Δd_h in the hydrodynamic diameter of **AuNPs@PEG-NH_2** and **AuNPs@PEG-mix** by 3.1 ± 0.9 nm and 3.9 ± 0.5 nm (respectively, Figure 2C-D). This indicated the formation of a protein corona around the particles after the adsorption of a single layer of **CTPR-Gd** proteins, equatorially oriented, as expected from the presence of PEG-NH_2 ligands in the AuNPs. Instead, a small decrease in size was observed after incubation of **AuNPs@PEG-Br** with **CTPR-Gd** ($d_{h,\ core+PEG+prot}$ = 20.5 ± 1.2 nm), indicating that PEG-Br prevents the formation of a stable protein corona. This decrease might be due to the constant hydrodynamic diameter of the NP and a slight increase in solution viscosity after protein addition, which is not accounted for by the automatic fitting process of the software.[49]

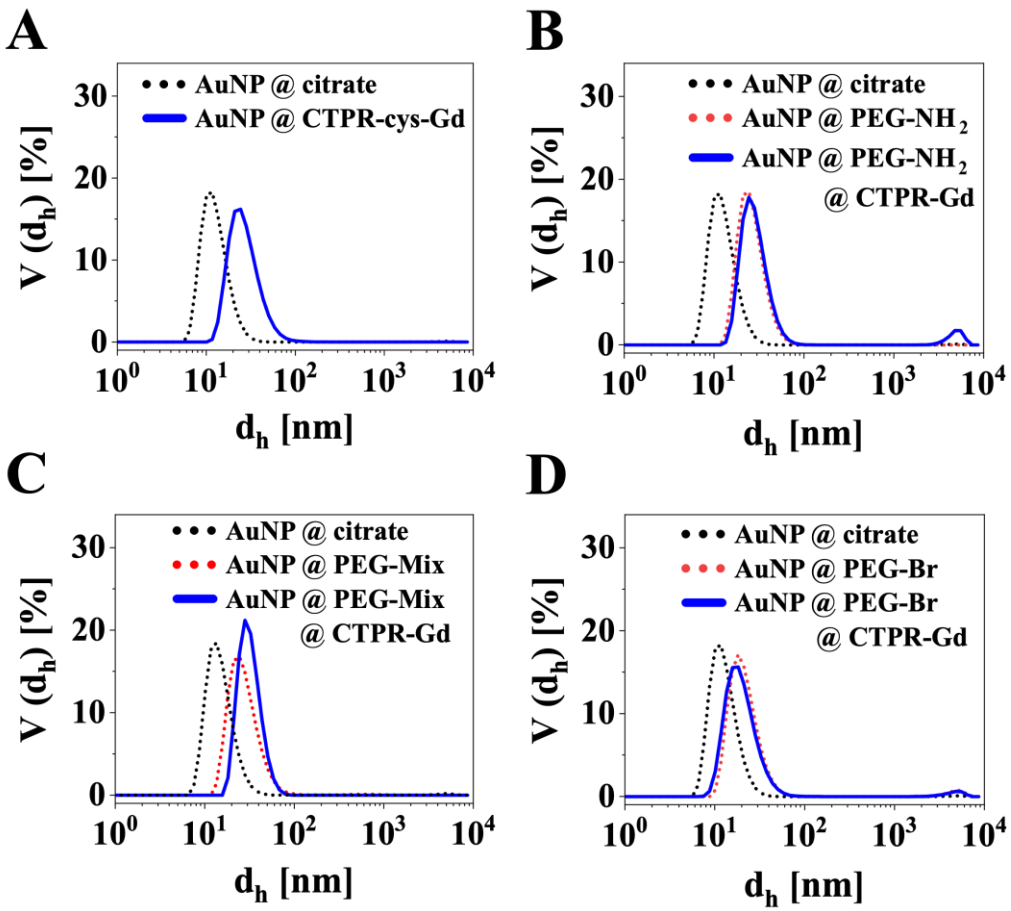

Figure 2: Volume-weighted V (d_h) hydrodynamic diameter d_h distribution of all gold nanoparticle formulations during various surface modification steps, measured by dynamic light scattering. A) covalently immobilised protein onto AuNP, and: B) amino pegylated AuNP (**AuNP@PEG-NH2**), C) PEGylated nanoparticle carrying 75% amino- and 25% bromine-terminated PEG ligands (**AuNP@PEG-mix**) and D) bromine terminated PEGylated AuNP (**AuNPs@PEG-Br**), in the absence or presence of **CTPR-Gd** proteins. The shown curves are averaged from three technical replicates. A consistent increase in hydrodynamic diameter is observed following PEGylation (red dots in B, C, D), indicating the successful surface modification. Further increases in the hydrodynamic diameter upon incubation **with CTPR-cys-Gd** or **CTPR-Gd**, respectively, indicating the formation of a protein corona. In contrast, no shift is observed for **AuNP@PEG-Br@CTPR-Gd**, suggesting the absence of a protein corona formation.

2.3. ASAXS of NP systems

The potential of ASAXS as a valid tool to probe the individual components of NPs was assessed using the systems previously described, which contained Au, Br or Gd respectively in their metal core, ligand layer or protein corona. This provided distinct X-ray contrasts, as the overall scattering from the sample (f) changed in proximity to the absorption edges of each of these

elements due to their different scattering coefficients (Equation 1). Near the absorption edge of an element, the energy (E)-dependent anomalous scattering correction (f^{Δ}) must be considered additionally to the energy-independent scattering (f^{0}).[39,50]

$$f = f^{0} + f^{\Delta} \quad \text{(Equation 1)}$$

$$f^{\Delta}(E) = f'(E) + i f''(E) \quad \text{(Equation 2)}$$

This correction term is composed of a real component (f'), which accounts for changes in the phase velocity of the incident X-rays (Equation 2). This is known as the dispersion correction. The imaginary component (f'') is associated with the reduction of the scattered waves amplitude due to X-ray absorption. The scattering contributions in units of ϖ (relative number of electrons per atom) were extracted from National Institute of Standards and Applications[51] and illustrated for Au in Figure 3A, for Gd and Br in Figure S4 A, G.

As a result, it was possible to perform ASAXS from each sample (Figure 3 B, C, Figure S4) by acquiring spectra at four different energies in the proximity of the Au-L_3 edge (sensitive to Au cores), Br-K edge (sensitive to brominated ligand layers) or Gd-L3 edge (sensitive to both types of CTPR proteins). Three spectra were acquired at energies before (starting around 100 eV before) the specific absorption edge and one around the edge studied (≤ 10 eV). While beam damage controls confirmed sample stability at higher X-ray energies (Au edge, cf. SI chapter 12), no equivalent tests were performed at the Gd edge. Therefore, subtle beam-induced alterations at lower energies, particularly affecting the low-q region (as seen in Figure 4C, SI Table S3), cannot be fully ruled out, and future ASAXS studies should include explicit beam damage controls at all energies probed.

Initial fitting of the ASAXS data to a single hard-sphere model allowed to obtain the radius of gyration (r_g) for each sample at the different energies studied. As anticipated and consistent with previous reports,[43] the r_g calculated from spectra collected near Au-L_3 edge increased due to anomalous scattering contributions from the Au core, while those collected near Br-K or Gd-L_3 edges decreased due to the contributions from external ligand layer or proteins (Fig 3D-F and Table S2). When the incident X-ray energy approaches the Au-L_3 edge, the contrast between the Au core and the ligands decreases, causing a portion of the ligand to become discernible as part of the sphere in the fitting procedure. This leads to an apparent increase in the particle size. Conversely, the decrease in scattering intensity near the absorption edge of the shell material, Br and Gd, results in a reduction in the contributions of the shell and eventually, the particle size. These results confirmed the structural conformation of our NP systems, and validated our experimental acquisition protocols. Then, the resonant scattering contributions

(I_R) of individual elements within the NPs were extracted using the Stuhrmann equation as previously described,[52] obtaining specific scattering patterns to characterise each of the components of NPs.

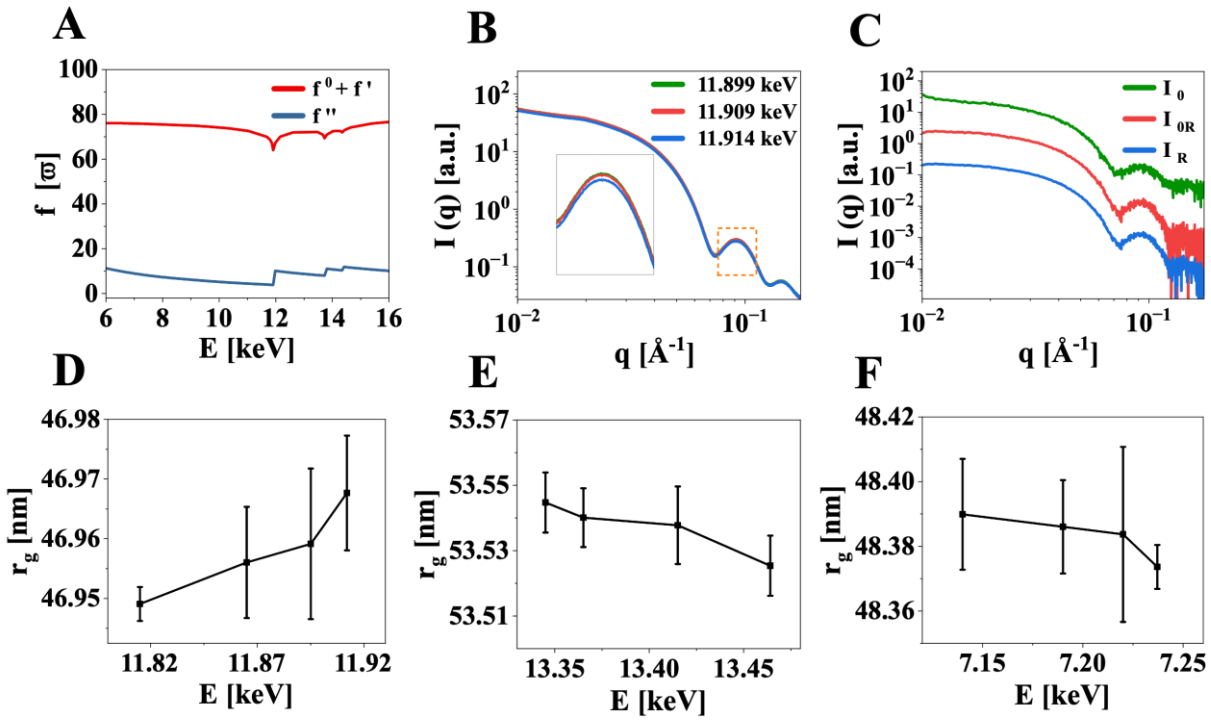

Figure 3: A) Real (red) and imaginary (blue) components of the atomic scattering coefficient of Au depending on the energy of the incident X-ray energy, showing the characteristic probed resonance at the Au-L_3 absorption edge (~11.919 keV). B) Measured scattering curves I(q) of **Au@PEG-mix@CTPR-Gd** acquired near the Au-L_3 edge, illustrating subtle changed in the scattering profile due to anomalous dispersion. C) Discrimination between resonant (I_R), non-resonant (I_0) and mixed (I_{0R}) scattering contributions from scattering curves in B) obtained by Stuhrmann equation. The radius of gyration r_g for **Au@PEG-Br@CTPR-Gd** was determined at incident energies near the Au-L_3 (11.919 keV - D), Br-K (13.474 keV - E) or Gd-L_3 (7.243 keV - F) edges. The energy dependent variation in r_g reflects the contribution of the respective element to the overall electron density distribution. The error bars represent the uncertainty derived from a single dataset and indicate the mathematical error in the calculation.

2.3.1. Analysis by model based fitting

The different I_R curves obtained were evaluated based on a core-shell model (Figure 4 and Table S3), which was expected for the immobilisation of PEG polymers or **CTPR-cys-Gd** on an Au core and subsequent adsorption or not of a corona of proteins. As the model based fitting procedure provides a radius of gyration of the gold nanoparticle core ($r_{g,core}$), we subsequently converted to a physical diameter ($d_{core} = 2 \times r_{g,core} \times \sqrt{(5/3)}$) throughout this section for better

comparison to diameters obtained by TEM and DLS. This conversion holds for a homogenous mass distribution of a sphere, which can be reliably assumed in the case of AuNPs. Moreover, the fitting provides a shell thickness. When probed at the Gd edge this shell is assigned to a layer of proteins ($\Delta r_{shell(prot)}$), and while analysing data sensitive to Br this shell thickness corresponds to the PEG layer ($\Delta r_{shell(PEG)}$). To obtain the overall diameter of the system, and to compare it to the results obtained by DLS, we added twice the shell thickness to the NP core diameter ($d_{core+prot} = d_{core} + 2 \times \Delta r_{shell(prot)}$), ($d_{core+PEG} = d_{core} + 2 \times \Delta r_{shell(PEG)}$), respectively, or in case of the triple segmented particle ($d_{core+PEG+prot} = d_{core} + 2 \times \Delta r_{shell(PEG)} + 2 \times \Delta r_{shell(prot)}$).

Fitting of the data from **AuNP@CTPR-cys-Gd** sample to this model indicated an Au core diameter of d_{core} = 12.0 ± 0.2 nm (obtained from data sensitive to Au-L_3) and an overall diameter of the NP system of $d_{core+prot}$ = 28.4 ± 0.6 nm (obtained from data sensitive to Gd-L_3). These values are in agreement with those obtained by DLS and TEM, and validate the use of ASAXS at the Gd-L_3 edge to study Gd labelled CTPR proteins. Similar results were obtained when using the same model to fit the resonant scattering curves obtained from **AuNP@PEG-NH_2@CTPR-Gd**, which yielded an Au core size of d_{core} = 12.8 ± 0.06 nm, and a protein corona thickness of $\Delta r_{shell(prot)}$ = 4.0 ± 2.1 nm. Once more, values were equivalent to results obtained from DLS and TEM, but the lack of contrast in the ligand layer did not allow to characterise the full system. The use of NPs carrying PEG-Br solved this issue, and allowed us to characterise the ligand layer around the particles (Figure 4 and Table S3). Fitting of ASAXS data from **AuNP@PEG-Br@CTPR-Gd** and **AuNP@PEG-mix@CTPR-Gd** to the core-shell model gave Au core sizes of d_{core} = 12.6 ± 0.1 nm and 12.0 ± 0.1 nm (respectively). The corresponding diameters covering both, the core and ligand were determined to be $d_{core+shell(PEG)}$ = 21.6 ± 0.2 nm and 28.0 ± 1.4 nm (respectively; obtained from data sensitive to Br-K). This showed good agreement with previous analysis by DLS and TEM, and confirmed further the convenience of using heavy element tags as ASAXS labels. Still, the fitting of ASAXS spectra from the same samples at the Gd-L_3 edge (which probe **CTPR-Gd** proteins) revealed a radius increase of $\Delta r_{shell(prot)}$ = 3.9 ± 0.4 nm for **AuNP@PEG-mix@CTPR-Gd** and 2.0 ± 0.3 nm for **AuNP@PEG-Br@CTPR-Gd.**

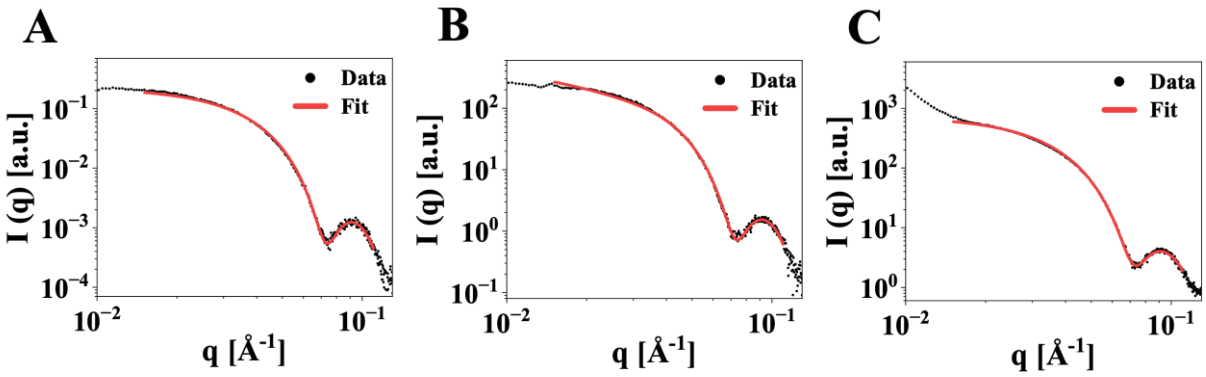

Figure 4: Resonant SAXS curves and core-shell model-based fits for AuNP@PEG-mix@CTPR-Gd at the absorption edges Au-L_3 (A), Br-K (B), and Gd-L_3 (C). Experimental scattering data (black dots) and corresponding core-shell model fits (red lines) are shown for each energy. The model provides a good fit at the Au-L_3 and Br-K edges, whereas at the Gd-L_3 edge, deviations occur at lower q-values. These deviations likely arise from minimal beam-induced alterations, leading to an increase in intensity at low q, as well as the presence of free CTPR-Gd in solution, which is not fully captured by the core-shell model. The chosen q-range (0.015 – 0.11 $Å^{-1}$) for all fits excludes possible alterations in the low-q region and reduces noise contributions at high q, ensuring a more robust comparison between different energies and samples.

This was unexpected, as DLS data suggested the formation of a protein corona of **CTPR-Gd** around **AuNP@PEG-mix**, but not **AuNP@PEG-Br**. Therefore, such finding may suggest two possible scenarios: 1) for **AuNP@PEG-Br@CTPR-Gd** ASAXS at the Gd-L_3 edge might be dominated by background noise from free **CTPR-Gd** proteins in solution; or 2) the proteins might be intercalated within the PEG layer of **AuNP@PEG-Br**, without altering the overall hydrodynamic diameter of the particles. It is worth mentioning that proteins with strong interaction potential, can embed themselves within the PEG coatings around NPs.[53] Additionally, lower PEG densities can increase interchain spacing, which can facilitate penetration[54] and intercalation (due to hydrophobic interactions)[55,56] of proteins. Nevertheless, this is not the case in the samples analysed, so the result obtained brings doubt over the capacity of ASAXS to characterise a dynamic protein corona.

As such, we used a binary hard-sphere model to fit resonant scattering curves obtained at the Gd-L_3 edge (Table S4), in an attempt to simulate a scenario where the protein corona was not formed or did not alter significantly the hydrodynamic size of the NPs, and increase our sensitivity to free proteins in solution (Figure S5, detailed explanation in SI chapter 9). To quantitatively assess the quality of the fits, the reduced chi-square (χ^2/Npts) was calculated. In

this calculation, χ^2 is used to quantify the deviation between the experimental data points and the fit model, and (Npts) represents the total number of data points. This ensures a normalized and comparable goodness-of-fit evaluation throughout all datasets. Interestingly, the quality of the fit using this new model (shown as χ^2/N_{pts} in Table S4) depended on the sample analysed. Fitting based on a core-shell model was much better for **AuNP@CTPR-cys-Gd** and **AuNP@PEG-NH$_2$@CTPR-Gd** than that achieved by a binary hard-sphere model, but just marginally better for **AuNP@PEG-mix@CTPR-Gd** and equivalent for **AuNP@PEG-Br@CTPR-Gd**. Moreover, the size ($r_{g,prot,exp}$) obtained for the small sphere in those two samples (PEG-mix and PEG-Br) was 4.3 ± 2.0 nm and 4.8 ± 0.5 nm (respectively), while it was 16.7 ± 1.1 nm and 8.0 ± 0.1 nm for **AuNP@CTPR-cys-Gd** and **AuNP@PEG-NH$_2$@CTPR-Gd** (respectively). This suggested the presence of significant populations of free proteins in samples containing PEG-Br ligands, but not in those with static or strong dynamic protein coronas around them. However, when the ratio between the two spheres (*i.e.* large = NPs, small = free **CTPR-Gd** proteins) was calculated after fitting (see SI chapter 9 and Table S5), it revealed a ratio of 125.0 or 572.5 CTPR-Gd$_{free}$/NP respectively for **AuNP@PEG-mix@CTPR-Gd** and **AuNP@PEG-Br@CTPR-Gd**. As each sample contains ~ 500 CTPR-Gd$_{Tot}$/NP, this confirms that a corona is formed around **AuNP@PEG-mix** (but a significant fraction of **CTPR-Gd** is still free in solution) but not **AuNP@PEG-Br**. Applying this calculation to **AuNP@CTPR-cys-Gd** and **AuNP@PEG-NH$_2$@CTPR-Gd,** a ratio of 0.6 or 9.4 CTPR$_{free}$/NP is obtained (respectively), underlying the formation of a protein corona with nearly all CTPR interacting with the AuNPs. Still, while the core-shell model initially applied accounts explicitly for a protein layer surrounding the nanoparticles, it seems to be incapable to discriminate reliably between the free **CTPR-Gd** and those forming a protein corona around the AuNPs when there is a significant number of free proteins in the solution. The binary hard sphere model, by contrast, offers a clear and robust interpretation when free proteins dominate in solution, and even in the case of nearly exclusive corona formation, it still provides valuable information by indicating the absence of free proteins in the solution.

2.3.2. Analysis by pair distance distribution function

By performing pair distance distribution function (PDF) calculations from a scattering plot it is possible to obtain information about the size and structure of the species present in the sample. As previously shown when studying NPs,[43] the peak in the PDF represents the most frequent distance between the scatterers in the NP. Instead, the maximum x-value where the probability

P(x) > 0 indicates the maximum extension of the scatterers, and can therefore be interpreted as the effective size of the NP.

As such, PDFs were calculated for the different I_R obtained from ASAXS acquired at the Au-L_3 edge, Br-K edge or Gd-L_3 edge from each of the four NP samples, with the intention of validating the data obtained from the model-based fitting of the same resonant scattering curves (Figure 5 and Table S6).

PDFs from the I_R at the Au-L_3 edge revealed a maximum distance of scatterers between d_{core} = x = 12.5 to 13.0 nm over all four formulations, which was in agreement with previous TEM and DLS measurements and fitting based on core-shell models. For the other elements present in the samples, it is reasonable to assume that PDFs are mostly dominated by the structure of the AuNP core, while the contributions of the few scatterers in the surrounding PEG or protein corona (carrying in comparison small amounts of Br or Gd labels) are minimal. PDF from resonant scattering contributions obtained at the Br-K edge from NPs carrying PEG-Br yielded sizes (core including the the PEG shell) of $d_{core+PEG}$ = 21.1 nm and 21.0 nm for the ligand layers of **AuNP@PEG-mix** and **AuNP@PEG-Br** (respectively).

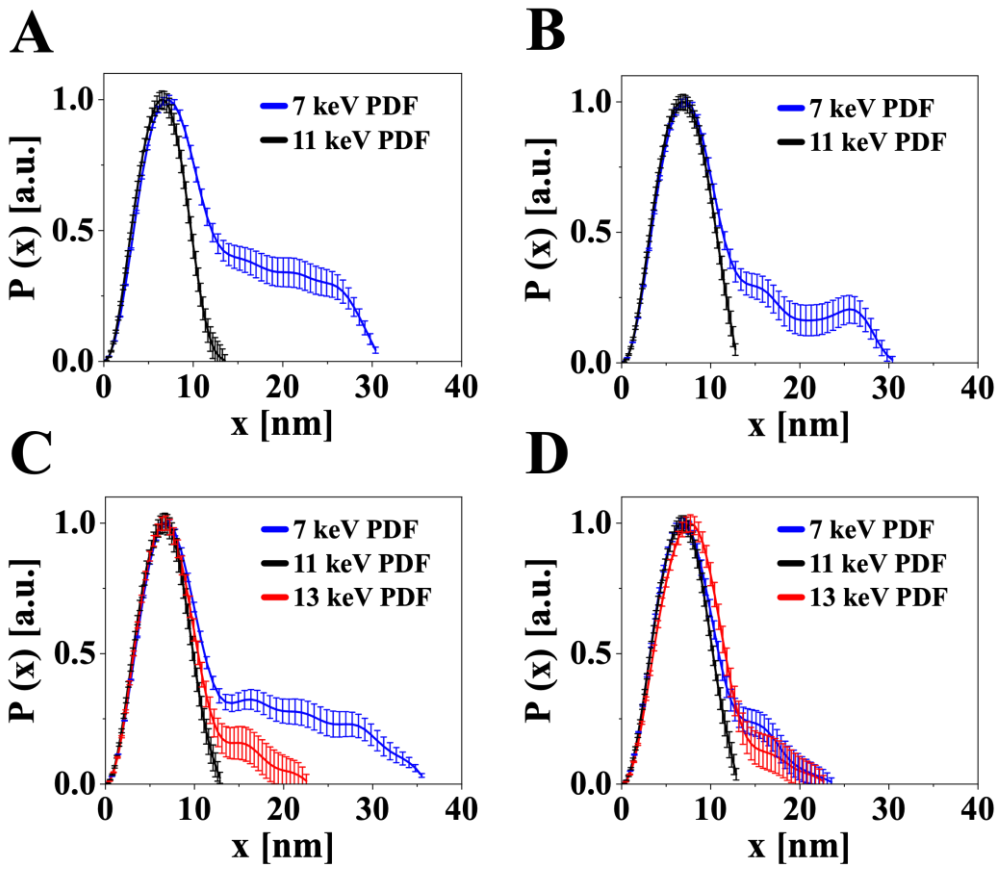

Figure 5: Normalised pair distance distribution functions (PDFs) as calculated from resonant SAXS curves obtained at the Au-L_3 (A), Br-K (B), and Gd-L_3 (C) edges from A) **AuNP@cys-CTPR-Gd**, B) **AuNP@PEG-NH$_2$@CTPR-Gd**, C) **AuNP@PEG-mix@CTPR-Gd** and D)

AuNP@PEG-Br@CTPR-Gd. Note that x means radial distance in this context and is therefore corresponding to a diameter (d) when assuming spherical geometry. Energy dependent changes in the shape of the PDF curves provide element-specific structural information. The extension of the PDF towards higher x values at 13 keV (near Br-K edge) reflects the contribution of the bromine atoms from the PEG-Br ligand (C, D). Additionally, the broader tail at 7 keV is attributed to the gadolinium signal from the **CTPR-Gd** protein, suggesting a size increasement of the formulations by the formation of a protein corona. The error bars represent the uncertainty derived from a single dataset and indicate the mathematical error in the calculation.

For **AuNP@PEG-Br** this was expected from previous DLS and ASAXS core-shell model based fitting calculations. It was smaller (around 6 nm) than expected from DLS and core shell fitting for **AuNP@PEG-mix**, as the PDF seemed to show the size of just the PEG-Br and not the full ligand layer around the NPs. Instead, PDFs from the resonant scattering at the Gd-L_3 edge agreed well with the sizes obtained previously by DLS and most cases of the core shell model fitting of the ASAXS data. This included diameters of $d_{core+PEG+prot}$ = 30.5 nm, 30 nm and 32.6 nm for **AuNP@CTPR-cys-Gd**, **AuNP@PEG-NH_2@CTPR-Gd** and **AuNP@PEG-mix@CTPR-Gd** (respectively). However, the maximum distance at the PDF for the **AuNP@PEG-Br@CTPR-Gd** formulation was determined to be x = 21.0 nm, which supports the model of two independent solid spheres and the DLS in this system. Thus, from this comprehensive analysis we conclude that no protein corona formation was present in this sample, even though the core shell model suggested it.

2.4. Comparison of characterisation techniques and analysis methods

A systematic comparison of the different techniques and analysis methods employed herein it is essential to gain a comprehensive understanding of the feasibility of using ASAXS to characterise the different components of NPs. Table 1 summarises results from the four AuNP systems tested with TEM, DLS, and ASAXS using core-shell and binary hard sphere fitting models or PDF analysis. Observation of the data obtained confirms that ASAXS is capable of characterising accurately the different components of AuNPs when they are made or labelled with tags with high-Z elements. However, the method used to analyse the I_R data of the individual samples must be approached with caution.

Model-based fitting can provide crucial information on the samples quickly, but the use of the wrong fitting model can also lead to false interpretations. In our case, core-shell fitting models are particularly powerful and accurate for the analysis of the core of AuNPs and any other

component covalently bound directly to it. This made it possible to probe the ligand layers of **AuNP@PEG-mix** and **AuNP@PEG-Br** and the **CTPR-cys-Gd** proteins bound covalently around **AuNP@CTPR-cys-Gd**. Still, results obtained from core-shell fitting models when probing the corona of **CTPR-Gd** proteins around **AuNP@PEG** systems with Gd-L_3 ASAXS are not always consistent with those obtained with other techniques. Remarkably, model based fitting approaches seem only useful to probe molecules bound to AuNPs through non-covalent interactions when they constitute the dominant fraction of the overall population of the species in solution. This makes the results obtained for **AuNP@PEGs** unreliable and hampers the use of this type of analysis when the formation of the protein corona cannot be confirmed using other analytical methods.

Instead, the analysis of ASAXS data by PDF methods does not show any of these issues, as it represents ratios of distances between scatterers and depends more on the aggrupation of molecules than in the number of individual ones. Therefore, it is a much more reliable method to characterise the different components of AuNPs (independently of the nature of their interaction or the relative size of the population of the species studied) and should be preferred to the use of model based fitting approaches.

Table 1: Summary of diameters obtained by different methods for all samples. Values are expressed in nm. *Note: As **AuNP@PEG-NH_2@CTPR-Gd** did not offer any Br label for the PEG layer, the overall size obtained by ASAXS at Gd-L_3 edge was extrapolated from DLS result before protein introduction.

Method	**@CTPR-cys-Gd**	**@PEG-NH_2**	**@PEG-Mix**	**@PEG-Br**
TEM (d_{core})	12.0 ± 0.9	12.0 ± 0.9	12.6 ± 0.7	12.0 ± 0.9
DLS core ($d_{h,\ core}$)	12.9 ± 0.2	12.9 ± 0.2	13.1 ± 0.7	12.9 ± 0.2
ASAXS core shell Au L_3 edge (d_{core})	12.0 ± 0.2	12.8 ± 0.1	12.0 ± 0.1	12.6 ± 0.1
PDF Au L_3 edge (d_{core})	12.5	13.0	12.8	12.7
DLS AuNP@PEG ($d_{h,\ core+PEG}$)	-	26.8 ± 0.3	28.5 ± 1.0	21.7 ± 0.6
ASAXS core shell Br K edge ($d_{core+PEG}$)	-	-	28.0 ± 1.4	21.6 ± 0.2
PDF Br K edge ($d_{core+PEG}$)	-	-	21.0	21.0

DLS AuNP@CTPR-cys-Gd ($d_{h,\ core+prot}$) or AuNP@PEG@CTPR-Gd ($d_{h,\ core+PEG+prot}$)	29.0 ± 1.0	29.9 ± 0.9	32.0 ± 0.3	20.5 ± 1.2
ASAXS core shell Gd L_3 edge ($d_{core+prot}$ or $d_{core+PEG+prot}$)	28.4 ± 0.6	34.8 ± 4.1*	31.8 ± 2.1	25.6 ± 0.8
PDF Gd L_3 edge ($d_{core+prot}$ or $d_{core+PEG+prot}$)	30.5	35.0	32.6	21.0
2-sphere Gd L_3 edge: r_g small	16.7 ± 1.1	8.0 ± 0.1	4.3 ± 2.0	4.8 ± 0.5

2.5. Benchmarking against conventional techniques and methodological considerations

Benchmarking was performed against established techniques such as transmission electron microscopy and dynamic light scattering, which are routinely used to assess nanoparticle morphology and size. The ASAXS results showed strong agreement with DLS and TEM regarding core size and corona thickness, confirming its validity. However, ASAXS provides several distinct advantages. DLS, while widely used to determine the size of nanoparticles in solution, provides only ensemble-averaged hydrodynamic radii and is strongly biased toward larger or aggregated species. More critically, it lacks spatial resolution and is not possible in optically dense media due to its reliance on visible light scattering. This makes it an unsuitable technique for the *in situ* nanoparticle characterization in complex biological fluids or directly in tissue. TEM, on the other hand, enables direct visualization of nanoparticles but relies on sample preparation steps such as drying, staining, or embedding, which can also alter the native structures of the nanoparticle, ligand and/or protein corona. Furthermore, it is restricted to thin, electron-transparent samples and cannot be applied *in situ* to opaque or hydrated media. These limitations can be overcome with ASAXS, which enables label-specific, component-resolved structural analysis in fully hydrated samples, without invasive preparation, and under near-physiological conditions, as we have demonstrated here in a proof-of-principle study. Still, some methodological limitations of ASAXS need to be considered. First, the whole technique depends on the incorporation of high atomic number (Z) elements to generate the anomalous contrast, which may not always be compatible with desired biological functions or might even change the native state as well. Second, although no severe beam induced damage was observed under our conditions, this risk remains for sensitive biomolecules under prolonged synchrotron

exposure. Third, the requirement for synchrotron access currently limits its applicability to *in vitro* settings. However, the ability of X-rays to penetrate complex fluids presents opportunities for future implementations of the technique to more useful *ex vivo* setups.

3. Conclusions

Our study demonstrates that it is possible to evaluate different components of AuNPs, including metal core, ligand layer, and protein corona, using ASAXS. This was possible by labelling each of them with individual tags with different high-Z elements that provided X-ray contrast allowing to obtain element specific SAXS patterns. Four NP systems with different surface chemistry and diverse capacity to form a protein corona around them were analysed using different methods, and the results obtained were validated using data obtained previously with other techniques. Comparison of results from ASAXS with those from TEM, DLS and zeta-potential suggests that PDF based analysis of the ASAXS data is preferred to model based fitting in most cases, especially if no validating techniques are available. Nevertheless, ASAXS is a valid tool to characterise the different structural properties of complex NP systems. Moreover, the use of X-rays for acquisition might help to reduce background noise when studying the nanomaterials in complex biological fluids, which encourage future translation of ASAXS approaches for *ex vivo* or even *in vivo* studies.

4. Experimental

4.1. Materials

Sodium citrate (Sigma), Gold (III) chloride trihydrate (Sigma), Ethylenediaminetetraacetic acid disodium salt (EDTA, Sigma), Citric Acid (Sigma), Bromine-PEG-thiol (2 kDa, BiopharmaPEG), Amine-PEG-thiol (3 kDa, Rapp Polymere), Dithiothreitol (Sigma), Phosphate buffered saline tablets (Fisher Bioproducts). Protein expression: pProEx-HTA vector (Thermo Fisher), OverExpress™ C41(DE3) Chemically Competent Cells (Sigma), isopropyl 1-β-d-thiogalactoside (IPTG; 99%; Thermo Fisher), Ampicillin, sodium salt (99%; Sigma), LB Lennox (99%; Sigma), DNase I (1 U µL-1; ThermoFisher), lysozyme (Thermo Fisher), cOmplete™ Protease Inhibitor Cocktail (Roche), Tobacco Etch Virus (TEV) protease (Expressed in the laboratory), glycerol (99%; Thermo Fisher), ethylenediaminetetraacetic acid (EDTA; 99%, Sigma), imidazole (99%; Thermo Fisher), sodium chloride (NaCl; 99%, Sigma), and sodium phosphate monobasic (NaH_2PO_4; 99%, Sigma), dithiothreitol (DTT; 97%; Sigma). HisTrap FF Ni-NTA (Cytiva). Gd-labelled CTPR: Gadolinium^{3+} chloride hexahydrate ($GdCl_3 \cdot 6H_2O$; Sigma Aldrich), PD-10 desalting columns packed with Sephadex G-25 resin (Cytiva).

4.2. AuNP synthesis

Gold nanoparticles were synthesised following a protocol published previously by Schulz et. al.[48] Shortly, 533 mL of a citrate buffer solution was prepared by mixing 400 mL sodium citrate (2.75 mM) with 133 mL 2.75 mM citric acid solution. The solution was boiled under stirring for 15 minutes, followed by the addition of 266 µL of aqueous EDTA solution (40 mM). After 5 minutes, 133 mL of a preheated (T ≅ 90 °C) solution of gold chloride (817.5 µM) was added. The new mixture resulting was stirred under boiling for 20 minutes before letting it cool down to room temperature. For covalent immobilisation of the protein, AuNPs were concentrated and washed thrice by using Amicon® spin filter units (100 kDa molecular weight cut-off (MWCO), 4,000 rcf, 60 s).

4.3. Protein expression, purification and characterisation

The consensus tetratricopeptide repeat (CTPR) proteins[57] used in this work were engineered through a cloning approach previously described[44–46], and are made of 11 CTPR repeats. To generate a metal binding protein, six of these CTPR repeats were designed to bear four histidine residues at non-conserved positions (2, 5, 6, and 9).[58] The gene for the CTPR protein was generated by block cloning using BamHI and BglII digestion.[59] The gene for the CTPR protein containing the C-terminal cysteine (CTPR-cys) was obtained by quick change site-directed mutagenesis.[60] The different genes were inserted into a pProEx-HTA vector, which provides an N-terminal His_6 tag and ampicillin resistance. DNA sequencing (Stab Vida) confirmed the engineered gene sequences. The resulting plasmids, containing either the CTPR or CTPR-cys genes, were introduced into *Escherichia coli* C41 cells by heat-shock transformation.

Bacterial cultures were grown at 37°C until their optical density reached 0.6–0.8. At this stage, protein expression was initiated by adding 0.6 mL of 1 mM IPTG, with subsequent overnight incubation at 20°C. Bacterial cells were collected by centrifugation at 4500 rpm and 20°C for 15 min and then resuspended in a lysis buffer containing 500 mM sodium chloride, 500 mM urea, and 50 mM Tris (pH 8.0). The cells were lysed using freeze-thaw cycles and sonication and posteriorly centrifuged at 10,000 rpm and 4°C for 1 h. The soluble protein fraction was purified using a HisTrap™ High-Performance affinity chromatography column (Cytiva).

The His_6 tag was cleaved using TEV protease, and the resulting protein dialysed against a buffer containing 500 mM sodium chloride, 50 mM Tris at pH 8.0 (cut-off of 6-8 kDa, SpectraPor®). The His_6 tag and TEV protease were removed via size-exclusion chromatography (HiLoad 16/600 Superdex 75 pg column, Cytiva). The protein was concentrated using centrifuge filters

with 10 kDa cut-off (Amicon) and the final concentration was determined by the absorbance at 280 nm and the Beer-Lambert law (ε_{CTPR} = 137980 M^{-1} cm^{-1} and $\varepsilon_{CTPR\text{-}Cys}$ = 137980 M^{-1} cm^{-1}). The expression and purification of the recombinant CTPR proteins was verified by sodium dodecyl sulfate-polyacrylamide gel electrophoresis (SDS-PAGE, Figure S3 A) and Matrix Assisted Laser Desorption Ionisation – Time of Flight (MALDI-ToF, Figure S3 B, and D) and its secondary structure was analysed by circular dichroism (CD, Figure S3 C).

The mass spectra were acquired on a MALDI/TOF-TOF MS neofleX (Bruker) in positive reflection mode. The sample was prepared by mixing 1 µL of sample with 4 µL of a saturated solution of alpha-cyano-4-hydroxycinnamic acid solution (in 70/30 acetonitrile/water with 0.1% TFA). The mixture was then allowed to dry before measurement.

The CD spectra were acquired in a JASCO J-815 CD spectrometer using a quartz cuvette with 1 mm path length. The proteins were measured at a concentration of 5 µM.

Both proteins were labelled with Gd following a protocol previously described.[27,61] 1 mL of protein solution (20 µM) was mixed with a sixfold excess of $GdCl_3$ solution. The protein and gadolinium salt mixture were incubated at 37°C with shaking at 800 rpm for 30 min, after which 0.6 µL of NaOH (1 M) were added. The incubation was then continued overnight under the same conditions. The labelled proteins were finally purified using a PD-10 desalting column. The protein concentration was measured using the Bradford assay (Thermofisher), and the presence of Gd was verified by ICP-MS.

4.4. Surface modifications of AuNPs

For the PEGylation of the citrate-capped AuNPs, first PEG stock solutions were prepared in miliQ water (c_{PEG} = 10 mg/mL). Then, the PEG-containing solution was added rapidly under stirring to citrate stabilised AuNPs at a ratio of 10 PEG per nm^2 of Au surface. The gold surface was calculated based on diameter d_c of citrate AuNPs obtained from TEM and assuming the NPs as solid spheres. The concentration of citrate AuNPs was determined by measuring Au concentration by inductively coupled plasma–mass spectrometry (ICP-MS) and considering cubic closest packing in spheres with a diameter based on TEM examination. The particles were subsequently stirred overnight and cleaned by three rounds of centrifugation (20,000 g, 30 min), replacing the supernatant with fresh miliQ water. Covalent immobilisation of **CTPR-cys-Gd** bearing a terminal cysteine residue was carried out *via* thiol-gold coupling (Au-S) chemistry by adjusting previously published protocols.[62–64] 7.5 nmol of the protein was mixed with 5 µmol of dithiothreitol (DTT) in 500 µL phosphate-buffered saline (PBS) and incubated for 5 minutes. The protein was cleaned by size exclusion chromatography, taken up in 1 mL of

miliQ water, and 300 µL of citrate stabilised AuNPs (100 nM) was added. The mixture was left at 4°C overnight, followed by three repetitions of a cleaning procedure *via* centrifugation (25,000 rcf, 10 min) and replacing the supernatant with miliQ.

4.5. Characterisation

To assess the hydrodynamic diameter d_h of the hybrid particles, dynamic light scattering (DLS) was used. For this, nanoparticles were diluted in miliQ water to an absorbance of 0.2 at 450 nm and measured in plastic UV cuvettes (Sarstedt) with a Zetasizer (Malvern Panalytical, UK) using a 633 nm He-Ne laser. For zeta-potential determination of the particles by laser Doppler anemometry (Zetasizer, Malvern Panalytical, UK), the samples were diluted in miliQ water. The results of DLS and ζ -potential presented, are expressed as mean and standard deviation from three individual runs. UV-vis absorbance spectrometry (Agilent Varian Cary 5000, Santa Clara, USA) was conducted by diluting the samples in miliQ water until a maximum peak absorbance between 0.2 and 1.0 was reached. Transmission electron microscopy (TEM) was carried out at a JEOL JEM1011 (Akishima, Japan). TEM samples were prepared by dropping 10 µL of AuNPs solutions onto carbon-coated copper meshed grids that were then air-dried. For ICP-MS, samples were digested overnight in three different dilutions in freshly prepared aqua regia (HCl:HNO3; vol:vol = 3:1). Subsequently, the sample was diluted in 2 vol.% HNO3 and injected in an Agilent 7700 series ICP-MS. The machine was calibrated for 197Au and 158Gd using a multi element standard (Carl Roth) with 9 known concentrations between 0-2500 ppb. A linear regression of the obtained counts per second versus the known concentrations was performed, and a regression coefficient ≥ 0.999 was obtained for all measurements.

4.6. ASAXS Experiments

X-ray scattering experiments were performed at the SAXSMAT beamline P62 at Petra III at DESY, Hamburg.[65] **AuNP@CTPR-cys-Gd** were placed immediately after cleaning filled inside 1 mm diameter quartz capillaries, 0.01 mm wall thickness. The Au concentration was determined by ICP-MS to be 196 µg/mL. The different PEG-bearing AuNPs were mixed with an excess of 500 proteins *per* AuNP, and incubated at room temperature for at least 1 h, before transferring them in identical quartz capillaries. The Au concentration in the capillaries, determined by ICP-MS, was 446 µg/mL for **AuNP@PEG-mix@CTPR-Gd**, 150 µg/mL for **AuNP@PEG-Br@CTPR-Gd**, and 150 µg/mL for **AuNP@PEG-NH_2@CTPR-Gd**. SAXS data were collected at room temperature and ambient pressure with a monochromatic beam

focused to 300 x 300 µm^2 (Flux ~ 5 x 10^{12} ph/s at sample) and using an Eiger2 X 9M detector at a distance from the sample of 5.9778 m (for Au-L_3 and Br-K measurements) or 2.8184 m (for Gd-L_3 measurements). Each sample was measured in five repetitions, with lateral offset to avoid beam-induced alterations, for 0.5 s each at four energies before or at the Au-L_3 edge (11,815 eV; 11,865 eV, 11,895 eV; 11,912 eV), Br-K edge (13,345 eV; 13,365 eV; 13,415 eV; 13,464 eV) and Gd-L_3 edge (7,140 eV; 7,190 eV; 7,220 eV; 7,237 eV) using a Si(111) monochromator. Probing parameters (dwell time and flux) were initially probed to confirm no beam induced alteration of the samples (SI chapter 12). Azimuthal integration of the 2D scattering patterns was performed in a Python environment based on the PyFAI library.[66] Resonant scattering contributions were extracted following mathematical calculations, introduced by Sturmann et al., and Goerigk et al. [52,67–69] The resonant scattering curves were consecutively evaluated in the q range from $0.015 - 0.11$ Å^{-1} using a differential evolution adaptive metropolis (DREAM) model-based fitting approach in SasView V5.0.6.[70–72] As goodness of fit parameter, a reduced chi-square statistics was employed (χ^2/Npts).[73]

Author contributions

Conceptualisation, A.L.C., W.J.P. and C.S.-C.; methodology, M.S., L.K. and C.S.-C.; validation, M.S.; formal analysis, M.S., L.K.; investigation, M.S., L.K., G.G., X.S, S.H., and C.S.-C.; resources, M.S. and G.G.; data curation, M.S., X.S., S.H., L.K., C.S.-C.; writing—original draft preparation, M.S., L.K., W.J.P. and C.S.-C.; writing—review and editing, M.S., L.K., G.G., X.S, S.H., D.K., A.L.C., W.J.P. and C.S.-C.; visualisation, M.S., L.K.; software, L.K., X.S, S.H.; supervision, A.L.C., D.K., W.J.P. and C.S.-C.; project administration, C.S.-C.; funding acquisition, A.L.C., D.K., W.J.P. and C.S.-C. All authors have read and agreed to the published version of the manuscript.

Acknowledgements

We acknowledge DESY (Hamburg, Germany), a member of the Helmholtz Association HGF, for the provision of experimental facilities. Parts of this research were carried out at the SAXSMAT beamline P62 at PETRA III at DESY, Hamburg. Beamtime was allocated for proposal I20210668EC. This work was funded by the Cluster of Excellence ‘Advanced Imaging of Matter’ of the Deutsche Forschungsgemeinschaft (DFG)-EXC 2056-project ID 390715994 (to M.S., L.K., D.K. and W.J.P.). This research was supported by the European Research Council (LINCHPIN project, grant no. 818941 to DK, and ERC-2022-PoC1-NanoImaging-101069356 to ALC). This work was performed under the support of the Severo Ochoa Centres

and Maria de Maeztu Units of Excellence Program of the Spanish State Research Agency – Grant No. CEX2018-000867-S (DIPC) and MDM-2017-0720 (CIC biomaGUNE). The authors thank the Spanish State Research Agency (grant PID2020-118176RJ-I100 to CSC, grants PID2022- 137977OB-I00 and PDC2022-133345-I00-ProIMAGE to ALC), and the Gipuzkoa Foru Aldundia (Gipuzkoa Fellows program; grant number 2019-FELL-000018-01/62/2019 to CSC) for financial support. G.G. thanks "la Caixa" Foundation (ID 100010434, fellowship: LCF/BQ/DI20/11780020). Additionally, we would like to thank Dr. Florian Schulz for TEM examinations and Jinrui Li for additional ICP-MS measurements.

Conflicts of interest

There are no conflicts to declare.

Data availability

A data availability statement (DAS) is required to be submitted alongside all articles. Please read our full guidance on data availability statements for more details and examples of suitable statements you can use.

Notes

[#] Although 3.8 nm width (= d_{prot}) would suggest an ~11 nm² footprint on a flat surface, binding solely via the terminal cysteine likely stretches the protein on the curved AuNP. Additionally, a spherical shell model like the one used in this report, with 6 nm AuNP core and 9.9 nm protein length as outer radius, provides ≈15,932 nm³ available volume. Assuming each protein occupies ~112 nm³, up to ~142 proteins could pack in such shell. Thus, the observed ~71 proteins per AuNP and ~6.4 nm² footprint seems reasonable.

References

[1] A. C. Anselmo, S. Mitragotri, *Bioeng Transl Med* **2019**, *4*, DOI 10.1002/btm2.10143.

[2] Y. Barenholz, *Journal of Controlled Release* **2012**, *160*, 117.

[3] G. Zhang, T. Tang, Y. Chen, X. Huang, T. Liang, *Signal Transduct Target Ther* **2023**, *8*, DOI 10.1038/s41392-023-01579-1.

[4] S. R. D'Mello, C. N. Cruz, M. L. Chen, M. Kapoor, S. L. Lee, K. M. Tyner, *Nat Nanotechnol* **2017**, *12*, 523.

[5] T. Anchordoquy, N. Artzi, I. V Balyasnikova, Y. Barenholz, N. M. La-Beck, J. S. Brenner, W. C. W. Chan, P. Decuzzi, A. A. Exner, A. Gabizon, B. Godin, S. K. Lai, T. Lammers, M. J. Mitchell, S. M. Moghimi, V. R. Muzykantov, D. Peer, J. Nguyen, R.

Popovtzer, M. Ricco, N. J. Serkova, R. Singh, A. Schroeder, A. A. Schwendeman, J. P. Straehla, T. Teesalu, S. Tilden, D. Simberg, *ACS Nano* **2024**, *18*, 13983.

[6] C. Carnovale, G. Bryant, R. Shukla, V. Bansal, *ACS Omega* **2019**, *4*, 242.

[7] G. Sonavane, K. Tomoda, K. Makino, *Colloids Surf B Biointerfaces* **2008**, *66*, 274.

[8] A. Woźniak, A. Malankowska, G. Nowaczyk, B. F. Grześkowiak, K. Tuśnio, R. Słomski, A. Zaleska-Medynska, S. Jurga, *J Mater Sci Mater Med* **2017**, *28*, 1.

[9] B. D. Chithrani, A. A. Ghazani, W. C. W. Chan, *Nano Lett* **2006**, *6*, 662.

[10] X. Xie, J. Liao, X. Shao, Q. Li, Y. Lin, *Sci Rep* **2017**, *7*, DOI 10.1038/s41598-017-04229-z.

[11] K. F. Pirollo, E. H. Chang, *Trends Biotechnol* **2008**, *26*, 552.

[12] Y.-Q. Chen, M.-D. Xue, J.-L. Li, D. Huo, H.-M. Ding, Y. Ma, *ACS Nano* **2024**, *18*, 6463.

[13] C. Guo, H. Yuan, Y. Wang, Y. Feng, Y. Zhang, T. Yin, H. He, J. Gou, X. Tang, *Adv Drug Deliv Rev* **2023**, *200*, 115044.

[14] N. Kamaly, O. C. Farokhzad, C. Corbo, *Nanoscale* **2022**, *14*, 1606.

[15] M. P. Monopoli, C. Åberg, A. Salvati, K. A. Dawson, *Nat Nanotechnol* **2012**, *7*, 779.

[16] C. D. Walkey, J. B. Olsen, F. Song, R. Liu, H. Guo, D. W. H. Olsen, Y. Cohen, A. Emili, W. C. W. Chan, *ACS Nano* **2014**, *8*, 2439.

[17] Y. Li, N. A. Monteiro-Riviere, *Nanomedicine* **2016**, *11*, 3185.

[18] C. Corbo, R. Molinaro, A. Parodi, N. E. Toledano Furman, F. Salvatore, E. Tasciotti, *Nanomedicine* **2016**, *11*, 81.

[19] C. Marques, M. J. Hajipour, C. Marets, A. Oudot, R. Safavi-sohi, M. Guillemin, G. Borchard, O. Jordan, L. Saviot, L. Maurizi, *ACS Nano* **2023**, *17*, 12458.

[20] S. Roy, Z. Liu, X. Sun, M. Gharib, H. Yan, Y. Huang, S. Megahed, M. Schnabel, D. Zhu, N. Feliu, I. Chakraborty, C. Sanchez-Cano, A. M. Alkilany, W. J. Parak, *Bioconjug Chem* **2019**, *30*, 2751.

[21] O. Vilanova, J. J. Mittag, P. M. Kelly, S. Milani, K. A. Dawson, J. O. Rädler, G. Franzese, *ACS Nano* **2016**, *10*, 10842.

[22] M. Kokkinopoulou, J. Simon, K. Landfester, V. Mailänder, I. Lieberwirth, *Nanoscale* **2017**, *9*, 8858.

[23] C. Carrillo-Carrion, M. Carril, W. J. Parak, *Curr Opin Biotechnol* **2017**, *46*, 106.

[24] M. Carril, D. Padro, P. Del Pino, C. Carrillo-Carrion, M. Gallego, W. J. Parak, *Nat Commun* **2017**, *8*, DOI 10.1038/s41467-017-01826-4.

[25] A. M. Villacorta, A. Mielcarek, M. G. Martinez, H. Jorge, A. Henschke, E. Coy, V. Gomez-Vallejo, J. Llop, S. E. Moya, *Small* **2024**, *n/a*, 2309616.

[26] W. G. Kreyling, A. M. Abdelmonem, Z. Ali, F. Alves, M. Geiser, N. Haberl, R. Hartmann, S. Hirn, D. J. De Aberasturi, K. Kantner, G. Khadem-Saba, J. M. Montenegro, J. Rejman, T. Rojo, I. R. De Larramendi, R. Ufartes, A. Wenk, W. J. Parak, *Nat Nanotechnol* **2015**, *10*, 619.

[27] M. Skiba, G. Guedes, D. Karpov, N. Feliu, A. L. Cortajarena, W. J. Parak, C. Sanchez-Cano, *Int J Mol Sci* **2024**, *25*, DOI 10.3390/ijms25010528.

[28] L. F. Ferreira, A. S. Picco, F. E. Galdino, L. J. C. Albuquerque, J.-F. Berret, M. B. Cardoso, *ACS Appl Mater Interfaces* **2022**, *14*, 28559.

[29] C. Cassini, A. Wittmeier, G. Brehm, M. Denz, M. Burghammer, S. Köster, *J Synchrotron Radiat* **2020**, *27*, 1059.

[30] A. L. C. Conceição, V. Müller, E. C. Burandt, M. Mohme, L. C. Nielsen, M. Liebi, S. Haas, *Sci Rep* **2024**, *14*, DOI 10.1038/s41598-024-51945-4.

[31] C. Sanchez-cano, R. A. Alvarez-puebla, J. M. Abendroth, T. Beck, R. Blick, Y. Cao, F. Caruso, I. Chakraborty, H. N. Chapman, C. Chen, B. E. Cohen, D. P. Cormode, D. Cui, K. A. Dawson, G. Falkenberg, A. L. C. Conceic, C. Fan, N. Feliu, M. Gao, E. Gargioni, C. Glu, F. Gru, M. Hassan, Y. Hu, Y. Huang, S. Huber, N. Huse, Y. Kang, A. Khademhosseini, T. F. Keller, C. Ko, N. A. Kotov, D. Koziej, X. Liang, B. Liu, X. Ma, A. Machicote, W. Maison, S. Liu, Y. Liu, Z. Liu, L. M. Liz-marza, A. P. Mancuso, S. Megahed, B. Nickel, F. Otto, C. Palencia, S. Pascarelli, J. J. Richardson, A. Rosenhahn, A. Pearson, O. Pen, B. Qi, J. Ra, K. Rothkamm, M. Ru, M. K. Sanyal, R. E. Schaak, H. Schlemmer, M. Schmidt, O. Schmutzler, T. Schotten, F. Schulz, A. K. Sood, K. M. Spiers, T. Staufer, D. M. Stemer, A. Stierle, X. Sun, G. Tsakanova, P. S. Weiss, H. Weller, F. Westermeier, M. Xu, H. Yan, Y. Zeng, Y. Zhao, Y. Zhao, *ACS Nano* **2021**, *15*, 3754.

[32] F. Otto, X. Sun, F. Schulz, C. Sanchez-cano, N. Feliu, F. Westermeier, W. J. Parak, **2022**, *2201324*, 1.

[33] C. Körnig, T. Staufer, O. Schmutzler, T. Bedke, A. Machicote, B. Liu, Y. Liu, E. Gargioni, N. Feliu, W. J. Parak, S. Huber, F. Grüner, *Sci Rep* **2022**, *12*, 1.

[34] Z. Lin, X. Zhang, P. Nandi, Y. Lin, L. Wang, Y. S. Chu, T. Paape, Y. Yang, X. Xiao, Q. Liu, *Commun Biol* **2024**, *7*, 280.

[35] C. Xu, D. Xia, X. Zhang, Q. Yao, Y. Wang, C. Zhang, *TrAC Trends in Analytical Chemistry* **2024**, *171*, 117515.

[36] J. K. Mathiesen, J. Quinson, S. Blaseio, E. T. S. Kjær, A. Dworzak, S. R. Cooper, J. K. Pedersen, B. Wang, F. Bizzotto, J. Schröder, T. L. Kinnibrugh, S. B. Simonsen, L. Theil

Kuhn, J. J. K. Kirkensgaard, J. Rossmeisl, M. Oezaslan, M. Arenz, K. M. Ø. Jensen, *J Am Chem Soc* **2023**, *145*, 1769.
[37] K. Frank, N. A. Henke, C. Lampe, T. Lorenzen, B. März, X. Sun, S. Haas, O. Gutowski, A.-C. Dippel, V. Mayer, K. Müller-Caspary, A. S. Urban, B. Nickel, *Nat Commun* **2024**, *15*, 8952.
[38] R. Nakanishi, G. Machida, M. Kinoshita, K. Sakurai, I. Akiba, *Polym J* **2016**, *48*, 801.
[39] M. Sztucki, E. Di Cola, T. Narayanan, *Eur Phys J Spec Top* **2012**, *208*, 319.
[40] T. Narayanan, in *Soft Matter Characterization* (Eds: R. Borsali, R. Pecora), Springer Netherlands, Dordrecht, **2008**, pp. 899–952.
[41] P. Podsiadlo, S. G. Kwon, B. Koo, B. Lee, V. B. Prakapenka, P. Dera, K. K. Zhuravlev, G. Krylova, E. V Shevchenko, *J Am Chem Soc* **2013**, *135*, 2435.
[42] S. Haas, G. Zehl, I. Dorbandt, I. Manke, P. Bogdanoff, S. Fiechter, A. Hoell, *The Journal of Physical Chemistry C* **2010**, *114*, 22375.
[43] A. Yu. Gruzinov, M. A. Schroer, K. Manalastas-Cantos, A. G. Kikhney, N. R. Hajizadeh, F. Schulz, D. Franke, D. I. Svergun, C. E. Blanchet, *J Synchrotron Radiat* **2021**, *28*, 812.
[44] A. Aires, D. Maestro, J. Ruiz del Rio, A. R. Palanca, E. Lopez-Martinez, I. Llarena, K. Geraki, C. Sanchez-Cano, A. V. Villar, A. L. Cortajarena, *Chem Sci* **2021**, *12*, 2480.
[45] A. Aires, I. Llarena, M. Moller, J. Castro-Smirnov, J. Cabanillas-Gonzalez, A. L. Cortajarena, *Angewandte Chemie - International Edition* **2019**, *58*, 6214.
[46] A. Aires, M. Möller, A. L. Cortajarena, *Chemistry of Materials* **2020**, *32*, 5729.
[47] A. Aires, V. Fernández-Luna, J. Fernández-Cestau, R. D. Costa, A. L. Cortajarena, *Nano Lett* **2020**, *20*, 2710.
[48] F. Schulz, T. Homolka, N. G. Bastús, V. Puntes, H. Weller, T. Vossmeyer, *Langmuir* **2014**, *30*, 10779.
[49] F. Otto, F. Dallari, F. Westermeier, D. C. F. Wieland, W. J. Parak, F. Lehmkühler, F. Schulz, *Aggregate* **2024**, *5*, e483.
[50] B. L. Henke, E. M. Gullikson, J. C. Davis, *At Data Nucl Data Tables* **1993**, *54*, 181.
[51] National Institute of Standards and Technology, "X-Ray Form Factor, Attenuation, and Scattering Tables Main Page," **n.d.**
[52] H. B. Stuhrmann, in *Characterization of Polymers in the Solid State II: Synchrotron Radiation, X-Ray Scattering and Electron Microscopy* (Eds: H.H. Kausch, H.G. Zachmann), Springer Berlin Heidelberg, Berlin, Heidelberg, **1985**, pp. 123–163.
[53] Y. R. Perera, J. X. Xu, D. L. Amarasekara, A. C. Hughes, I. Abbood, N. C. Fitzkee, *Molecules* **2021**, *26*, DOI 10.3390/molecules26195788.

[54] J. Manson, D. Kumar, B. J. Meenan, D. Dixon, *Gold Bull* **2011**, *44*, 99.
[55] C. Li, J.-N. Zhang, J. Jin, W. Jiang, *Chinese Journal of Polymer Science* **2023**, *41*, 1879.
[56] B. Pelaz, P. del Pino, P. Maffre, R. Hartmann, M. Gallego, S. Rivera-Fernández, J. M. de la Fuente, G. U. Nienhaus, W. J. Parak, *ACS Nano* **2015**, *9*, 6996.
[57] K. B. Uribe, E. Guisasola, A. Aires, E. López-Martínez, G. Guedes, I. R. Sasselli, A. L. Cortajarena, *Acc Chem Res* **2021**, *54*, 4166.
[58] A. L. Cortajarena, A. Aires, A. Sousaraei, M. Möller, J. Cabanillas-Gonzalez, *Nano Lett* **2021**, *21*, 9347.
[59] A. L. Cortajarena, S. G. J. Mochrie, L. Regan, *Protein Science* **2011**, *20*, 1042.
[60] H. Liu, J. H. Naismith, *BMC Biotechnol* **2008**, *8*, 91.
[61] B. Zhang, H. Jin, Y. Li, B. Chen, S. Liu, D. Shi, *J Mater Chem* **2012**, *22*, 14494.
[62] A. R. Clapp, I. L. Medintz, H. Tetsuo Uyeda, B. R. Fisher, E. R. Goldman, M. G. Bawendi, H. Mattoussi, *J Am Chem Soc* **2005**, *127*, 18212.
[63] H. Mattoussi, J. Matthew Mauro, E. R. Goldman, G. P. Anderson, V. C. Sundar, F. V. Mikulec, M. G. Bawendi, *J Am Chem Soc* **2000**, *122*, 12142.
[64] K. L. Gurunatha, A. C. Fournier, A. Urvoas, M. Valerio-Lepiniec, V. Marchi, P. Minard, E. Dujardin, *ACS Nano* **2016**, *10*, 3176.
[65] S. Haas, X. Sun, A. L. C. Conceicao, J. Horbach, S. Pfeffer, *J Synchrotron Radiat* **2023**, *30*, 1156.
[66] J. Kieffer, J. P. Wright, *Powder Diffr* **2013**, *28*, S339.
[67] G. J. Goerigk, *Advances in Linear Algebra & Matrix Theory* **2013**, *03*, 59.
[68] G. Goerigk, K. Huber, N. Mattern, D. L. Williamson, *European Physical Journal: Special Topics* **2012**, *208*, 259.
[69] G. Goerigk, N. Mattern, in *J Phys Conf Ser*, Institute Of Physics Publishing, **2010**.
[70] M. Doucet, J. H. Cho, G. Alina, Z. Attala, J. Bakker, P. Beaucage, W. Bouwman, R. Bourne, P. Butler, I. Cadwallader-Jones, K. Campbell, T. Cooper-Benun, C. Durniak, L. Forster, P. Gilbert, M. Gonzalez, R. Heenan, A. Jackson, S. King, P. Kienzle, J. Krzywon, B. Maranville, N. Martinez, R. Murphy, T. Nielsen, L. O'Driscoll, W. Potrzebowski, S. Prescott, R. Ferraz Leal, P. Rozyczko, T. Snow, A. Washington, L. Wilkins, C. Wolf, **2023**, DOI 10.5281/zenodo.7581379.
[71] D. W. Marquardt, *Journal of the Society for Industrial and Applied Mathematics* **1963**, *11*, 431.
[72] Vrugt J. A., ter Braak C.J.F., Diks C.G.H., Robinson B. A., Hyman J. M., Higdon D., **2009**, *10*, 273.

[73] P. Bevington, D. K. Robinson, *Data Reduction and Error Analysis for the Physical Sciences*, McGraw-Hill Education, **2003**.